Evaluation of low-pressure flooded evaporator performance for adsorption chillers

Poovanna Cheppudira Thimmaiah, Amir Sharafian, Mina Rouhani, Wendell Huttema, Majid Bahrami*

Laboratory for Alternative Energy Conversion (LAEC), School of Mechatronic Systems Engineering, Simon Fraser University, BC, V3T 0A3, Canada

ABSTRACT

In an adsorption chiller, the refrigerant (water) operating pressure is low (0.5–5 kPa) and the cooling power generation of a flooded evaporator is affected by the height of water column. To resolve this issue, we experimentally investigate the performance of a flooded evaporator as a function of water height. The results show an optimum water height equal to 80% of the tube diameter leading to achieve the highest cooling power. Under this condition, the internal and external thermal resistances on the inside and outside of the evaporator tubes account for up to 73% of the overall thermal resistance. To reduce the internal thermal resistance, twisted and Z-type turbulent flow generators are incorporated into the evaporator tubes. The evaporator cooling power shows an increase by 12% and 58% when twisted tape and Z-type turbulators are used at a cost of an increase in the internal pressure drop by 2.5 and 14.5 times, respectively. The twisted tape and Z-type turbulators improve the average specific cooling power of the adsorption chiller by 9% and 47%, respectively. To reduce the external thermal resistance, the outside surface of the evaporator tubes is coated with porous copper. The coated evaporator increases the overall heat transfer coefficient by 1.4 times and improves the specific cooling power of the adsorption chiller by 48% compared to the uncoated tubes.

1. Introduction

Conventional vapor-compression refrigeration (VCR) technology has been the dominant technology of air conditioning systems for close to a century [1], but its environmental impact and high energy consumption are contrary to sustainable development. The synthetic refrigerants used in VCR systems contribute strongly to climate change and the energy consumption of heating, ventilation, and air conditioning (HVAC) equipment (including VCR systems) is considerable. For example, HVAC equipment contributed to over 38% of the total primary energy consumption in the U.S. buildings sector in 2013 [2]. In the transportation sector, VCR-based air conditioning (A/C) and refrigeration systems cause a 20% increase in fuel consumption [3].

In an internal combustion engine (ICE) of a light-duty vehicle 65–70% of the total fuel energy released is dissipated as waste heat through the engine coolant and the exhaust gas [4]. Besides, the need to reduce hydrofluorocarbon (HFC) use has stimulated interest in alternative HVAC systems such as waste heat-driven adsorption chillers. A portion of the waste heat of an ICE is sufficient to run an adsorption chiller and generate the cooling power required for the vehicle A/C applications (2–3.5 kW [5]). In addition to environmental benefits and energy savings, an adsorption chiller has the benefits of simple construction, no moving parts (except valves), no vibration, quiet operation, and low operating cost [6–9]. As a result, waste heat-driven adsorption cooling is a promising technology [2]. However, there are some technical limitations, including the need to maintain a high vacuum, and have a low specific cooling power (SCP) and coefficient of performance (COP). These limitations lead to a large size and heavy system compared to a conventional VCR system [10–12].

Designing a highly efficient and compact evaporator plays a significant role in reducing the mass and size of adsorption chillers. Water has traditionally been used as the refrigerant in adsorption chillers because of its high enthalpy of evaporation [13]. However, since the evaporator operates between 3 and 20 °C, its operating pressure (caused by water) varies between 0.76 and 2.34 kPa [14].

This low operating pressure mandates a special evaporator design as the accumulation of liquid water in the evaporator affects the evaporation rate. The water column in the evaporator creates a hydrostatic pressure [15] that increases the saturation temperature or boiling point, as shown in Fig. 1. For an evaporator operating at 1.22 kPa (10 °C), the hydrostatic pressure of water increases the saturation temperature to 25 °C at the depth of 20 cm, where the pressure (operating + hydrostatic) is 3.20 kPa. This temperature variation inside the evaporator reduces the generation of cooling power in an adsorption chiller. Under such circumstances, a conventional evaporator fails to perform efficiently.

Several low pressure (LP) evaporator technologies were studied in the literature: i) falling film, ii) capillary-assisted, and iii) flooded. The performance of different LP evaporators is compared in Table 1.

In a falling film evaporator, a refrigerant is sprayed on the outer surface of tubes. Falling film evaporators [18,26—28] provide large cooling capacities in a low footprint, but they need an equal distribution of refrigerant on the tubes, and have parasitic power consumption from an internal pump or circulator [29]. In a capillary-assisted evaporator, an enhanced tube with finely spaced external fins (or with fine porous coating) is positioned to be in contact with a pool of liquid refrigerant. Capillary action draws the refrigerant from the pool to cover the outside surface of the tube and produce uniform distribution of refrigerant along the tubes.

A comprehensive experimental analysis on capillary-assisted evaporators was conducted on several prototypes built in our laboratory at Simon Fraser University [30]. The results showed that the capillary-assisted tube with 0.635 mm fin spacing (40 fins per inch) and 14.45 mm inner diameter (ID) provided the best performance among a number of tested tubes [24]. However, the main bottleneck was the high internal heat transfer resistance of the liquid chilled water flowing inside the evaporator tubes [31].

Increasing the inlet chilled water mass flow rate to increase the internal heat transfer coefficient was not an option of interest because it results in a lower temperature difference between the inlet and outlet of the evaporator. To decrease the internal heat transfer resistance, tubes with smaller internal diameter were used (GEWA®-K-2615). This commercially available tube with 1 mm fin spacing (26 fins per inch) and 7.9 mm ID did not show capillary action as effectively as the tubes with 0.635 mm fin spacing. Therefore, the heat exchanger tube bundle was immersed in a pool of refrigerant (known as a flooded evaporator). The main challenge with this design was the hydrostatic pressure due to the water accumulation, and consequently, a higher external heat transfer resistance. Therefore, it is necessary to find an optimum refrigerant level in the flooded evaporator.

Most of the low pressure evaporation studies for varied filling levels were performed on flat plates with standard dimensions [32]. However, to the best of our knowledge, for a low finned tube evaporator, the impact of hydrostatic pressure due to the refrigerant height was overlooked in the design of LP flooded evaporators. This study attempts to fill this gap by evaluating the effect of refrigerant height in a flooded evaporator installed in an adsorption chiller. The turbulent flow generators are inserted into the evaporator tubes to improve the performance and reduce the internal heat transfer resistance. Finally, to improve the capillary action of the tubes and improve the flooded evaporator performance further, the outside surface of the evaporator tubes are coated with porous copper. The novelties in this paper are the effect of the porous copper coated LP evaporator and the effect of the turbulent flow generators on the specific cooling capacity of the adsorption chiller. This research demonstrates the utilization of a LP evaporator in an adsorption chiller where low-grade waste heat energy is available and LP evaporator are vital to the performance enhancement of an adsorption chiller.

2. Experimental study

A schematic of the LP flooded evaporator built with 12 horizontal tubes (12 pass) used in this study is shown in Fig. 2. Enhanced tubes with external fins are immersed in a pool of liquid water. Chilled water, provided by a temperature control system (TCS), was circulated inside the tubes and transferred heat to the pool of liquid refrigerant located on the outer surface the tubes. The tube bundle was placed horizontally at the bottom of the box to minimize the water height as shown in Fig. 2b. Type T thermocouples (Omega, model #5SRTC-TT-T-36-36) with an accuracy of 0.75% of reading were used to record the temperature at the locations shown in Fig. 2a. A pressure transducer (MKS Baratron® Capacitance Manometer, Type 722B) with an accuracy of 0.5% of reading was used to measure the pressure at the outlet of the evaporator. A differential pressure transducer with 0—206.8 kPa operating range (Omega, model #PX409-030DWUI) and accuracy of 0.5% of reading was used to record the pressure drop between the inlet and outlet of the chilled water line. A low-range differential pressure transmitter (0—1.25 kPa) and accuracy of 0.5% of reading (American sensor technologies, model #AST5100J00005H4Y500) was used to measure the height of the liquid refrigerant inside the evaporator. A positive displacement flow meter (FLOMEC, Model #OM015S001-222) with the accuracy of 0.5% of reading was employed to measure the mass flow rate of the chilled water.

The tests were conducted on a set of Wieland GEWA®-K-2615 tubes. The geometry and dimensions of this evaporator are
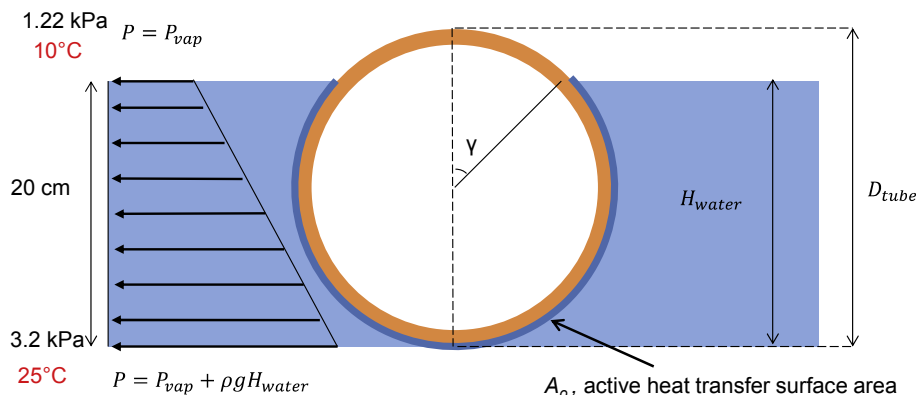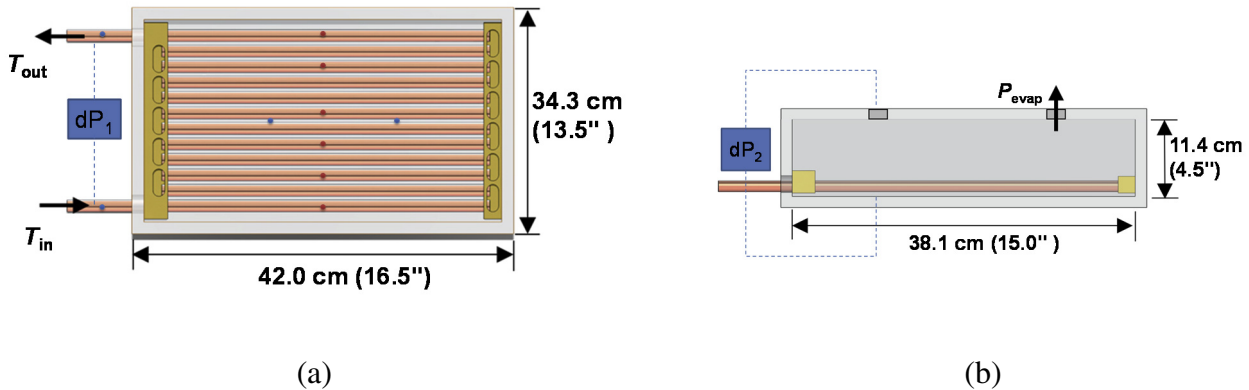

Fig. 1. Schematic of pool boiling on the surface of a tube.

Table 1
Performance of different LP evaporators with applications to adsorption chillers.

Ref.	Evaporator technology	Max. cooling power (kW)	Tube details	Operating pressure (kPa)	Evaporator material	Refrigerant	Thermal fluid	Heat transfer coefficient (W/m²·K)
Castro et al. [16]	Falling film	2.0	Length - 1.3 m OD - 0.63″ # of tubes - 36	1.0	Stainless steel	LiBr/Water	Water	—
Florides et al. [17]	Falling film/Vertical tube	1.0	Length - 1.0 m OD - 0.375″ ID - 0.32″ # of tubes - 11	0.9	Copper	LiBr/Water	Water	—
Li et al. [18]	Falling film	0.78	Length − 0.7 m OD - 0.63″ ID - 0.5″ to 0.57″ # of tubes - 36	1.0	Copper	Water	Water	Overall U: 3500 (Chilled water flow rate- 16.7 L per minute)
Sabir et al. [19—21]	Capillary-assisted on the inner surface of the tube	0.7—1.6	Length - 0.3 m OD - 1 $\frac{1}{8}$″ # of tubes - 9	1.5	Copper	Water	Air	Direct exchange type: 500—1000 [20] Internal powder coated: 3000 [20]
Schnabel et al. [14]	Partly flooded and partly capillary-assisted on the outer surface of the tube	1.2	Length - 0.4 m OD - 0.71″ # of tubes - 4	1.1—1.7	Copper	Water	Water	—
Xia et al. [22]	Capillary-assisted on the outer surface of the tube	0.45	Length - 0.36 m OD - 0.71″ # of tubes - 1	0.8—1.0	Copper	Water	Water	5500 (ΔT = 5 K, T_{sat} = 5 °C)
Lanzerath et al. [23]	Capillary-assisted on the outer surface of the tube	0.3—0.6	Total length - 2.00 m OD - 0.74″ ID - 0.52″	0.8—2.3	Copper	Water	Water	Overall U: 4250—6100 (Chilled water flow rate- 16 L per minute)
Thimmaiah et al. [24]	Capillary-assisted on the outer surface of the tube	0.3—0.4	Length - 0.39 m OD - ¾″ # of tubes - 4	0.5—0.8	Copper	Water	Water	Overall U: 800—1000 (Chilled water flow rate- 2.3—2.5 L per minute)
Castro et al. [25]	Flooded type	7.0	Length - 0.27 m OD - 0.39″ # of tubes - 16	1.1	Copper	Water	Water	

T_{out} dP$_1$ T_{in} 34.3 cm (13.5″) 42.0 cm (16.5″)

(a)

P_{evap} dP$_2$ 11.4 cm (4.5″) 38.1 cm (15.0″)

(b)

Fig. 2. The flooded evaporator: (a) top view and (b) side view. Red dots indicate the position of thermocouples on the tubes and blue dots indicate the position of thermocouples measuring the temperature of the liquid refrigerant. (For interpretation of the references to colour in this figure legend, the reader is referred to the web version of this article.)
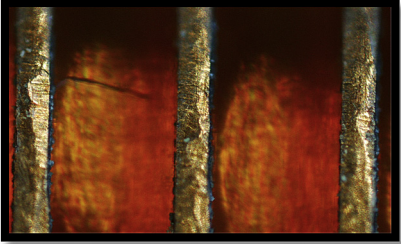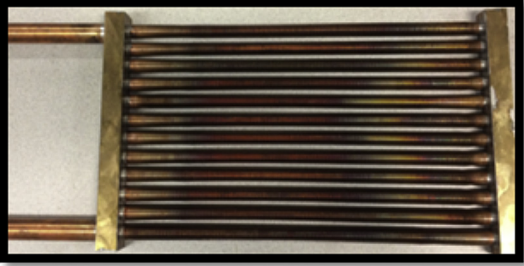
summarized in Table 2.

A schematic diagram and a photograph of the adsorption chiller experimental setup built in our laboratory are shown in Fig. 3. It consists of two adsorber beds, a condenser, expansion valve, and an evaporator. Four TCS provide and control the temperatures of these components. Further details of the two-bed adsorption chiller test setup can be found in Ref. [33]. The TCS connected to the evaporator was equipped with a variable speed pump to provide a constant temperature chilled water to the evaporator at different mass flow rates.

Before running the experiments, the adsorber beds coated with AQSOA FAM-Z02 adsorbent were heated using a 90 °C heating fluid for 8 h and simultaneously evacuated to be completely dried. The heating and cooling fluid inlet temperatures to the adsorber beds, and the coolant and chilled water inlet temperatures to the

condenser and evaporator were set, as listed in Table 3. An experiment at cyclic operating conditions was performed continuously until the dynamic behavior of the chiller became repetitive. At this stage, the adsorption cycle was repeated for three more times to ensure the reproducibility of the collected data.

To begin each experiment, the evaporator was evacuated, and then filled with water to immerse the evaporator tubes. A vacuum pump was used to evacuate the dissolved gases from the evaporator before the beginning of the experiment. The low-range differential pressure transmitter was used to measure the refrigerant level at the beginning of evaporation. When the temperatures and pressure inside the evaporator became constant, the control valves between the adsorber beds and evaporator were opened and the evaporator pressure was then set by the adsorption rate of the adsorber beds. To find the optimum level of refrigerant, the water

Table 2
Technical specifications of the enhanced tubes used for the experiments.

Evaporator name and details	5× zoom view	Photograph of the evaporator
GEWA®-K-2615 (Wieland Thermal Solutions) Copper Alloys C12200 Fin type: continuous and parallel fins OD: 1/2″ (12.7 mm) Fin height: 1.5 mm Root wall thickness under fins: 0.8 mm Inside surface area: 0.024 m²/m Outside surface area: 0.124 m²/m Number of tubes-12 Number of passes-12		
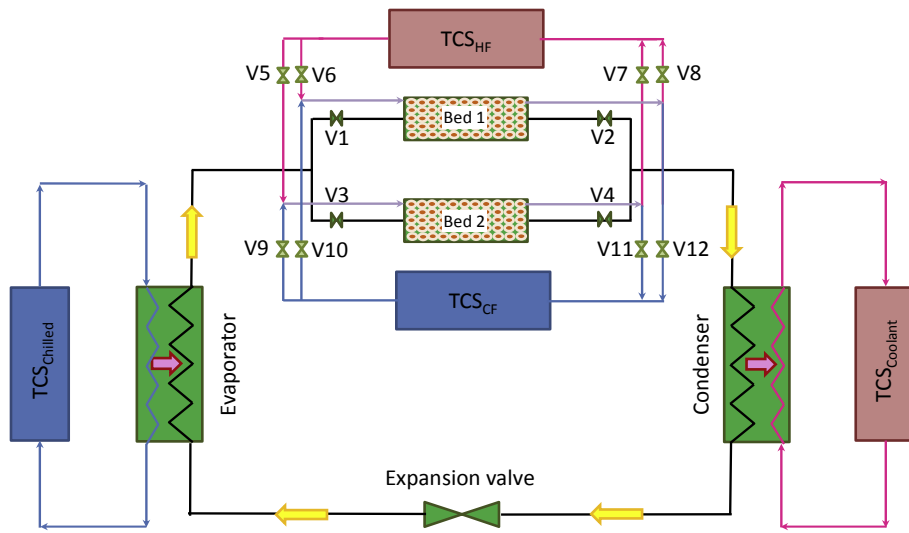
(a)
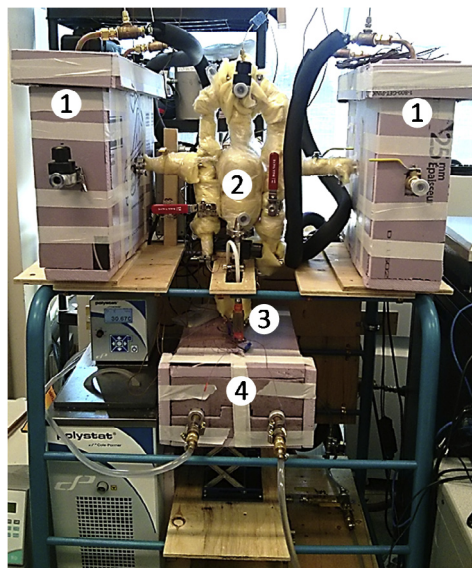
(b)

Fig. 3. (a) Schematic of the adsorption chiller experimental setup available at LAEC [33] and (b) two-adsorber bed adsorption chiller experimental testbeds, Numbers in (b): 1-adsorber bed(s), 2-condenser, 3-expansion valve, and 4-evaporator.

Table 3
Specifications and operating conditions of the adsorption chiller.

Parameter	Two-bed adsorption chiller
Working pairs	AQSOA FAM-Z02/water
Mass of adsorbent per adsorber bed (kg)	0.7
Adsorber bed heat transfer surface area, A_{bed}, (m²)	2.8
Metal mass of adsorber bed (kg)	2.87
Adsorber bed fin spacing (mm)	2.54
Adsorber bed fin dimensions (cm)	30.48 × 3.81 (12″ × 1.5″)
Heating fluid mass flow rate to adsorber bed (kg/s)	0.058 (4.1 L/min of silicone oil)
Cooling fluid mass flow rate to adsorber bed (kg/s)	0.062 (4.1 L/min of silicone oil)
Heat capacity of heating and cooling fluids (kJ/kg.K)	1.8
Condenser heat transfer surface area, A_{cond}, (m²)	2.0
Coolant water mass flow rate to condenser (kg/s)	0.052 (3.1 L/min)
Evaporator heat transfer surface area, A_{finned}, (m²)	0.49
Chilled water mass flow rate to evaporator (kg/s)	0.025 and 0.037 (1.5 and 2.5 L/min)
Heating fluid inlet temperature to adsorber bed (°C)	90
Cooling fluid inlet temperature to adsorber bed (°C)	30
Coolant water inlet temperature to condenser (°C)	30
Chilled water inlet temperature to evaporator (°C)	5/10/15/20
Cycle time (min)	20

level (H*) was varied from 0.2 to 1.0, where H* represents the ratio of water (refrigerant) height to the tube diameter. For a given experiment, the filling level H* was constant at every half cycle after the refrigerant refluxed from the condenser. For the rest of the tests, the water level was kept at the optimum level. Each experiment at respective filling level H* was repeated three times until reproducible temperatures and pressures were achieved. In this study, the average of the last two cycles was reported as the performance of the evaporator (or system).

3. Data analysis

The chilled water inlet and outlet temperatures, T_{in} and T_{out}, and the mass flow rate $\dot{m}_{in}$ were used to calculate the heat transfer rate from the chilled water flowing inside the tubes [34]:

$$\dot{q}_e = \dot{m}_{in} c_p (T_{in} - T_{out}) \tag{1}$$

The mean specific heat capacity at constant pressure from chilled water stream is considered. The total evaporation rate, $\dot{Q}_e$, is calculated by time averaging the heat flow rate:

$$\dot{Q}_e [W] = \frac{\int_{t_1}^{t_2} \dot{q}_e dt}{t_2 - t_1} \tag{2}$$

where t_1 and t_2 are the beginning and the end of the time when the temperatures in the evaporator remain constant. Finally, the overall evaporator heat transfer conductance, UA, is given by:

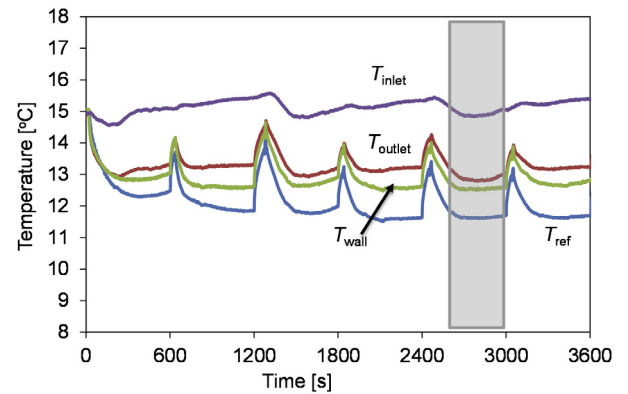$$UA = \frac{\dot{Q}_e}{\Delta \overline{T}_{LMTD}} \tag{3}$$

where A is the nominal surface area of the tubes and $\Delta \overline{T}_{LMTD}$ is the logarithmic mean temperature difference between the chilled water and the liquid refrigerant:

$$\Delta T_{LMTD} = \frac{T_{in} - T_{out}}{\ln\left(\frac{T_{in} - T_{sat}}{T_{out} - T_{sat}}\right)} \tag{4}$$

$$\Delta \overline{T}_{LMTD} = \frac{\int_{t_1}^{t_2} \Delta T_{LMTD} dt}{t_2 - t_1} \tag{5}$$
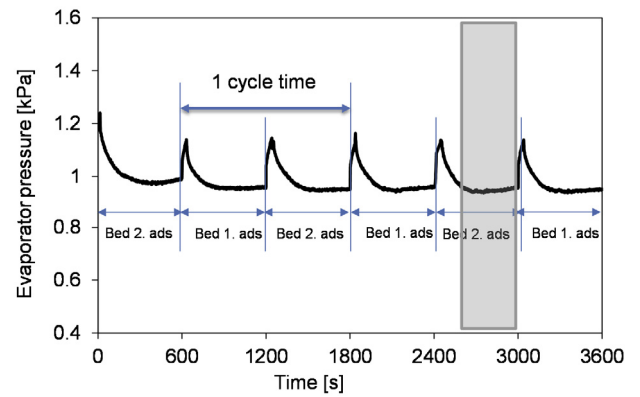
(a)

(b)

Fig. 4. Behavior of the evaporator at a chilled water inlet temperature of 15 °C vs. time: (a) evaporator pressure and (b) temperature at different locations in the evaporator.

with T_{sat} the refrigerant saturation temperature.

The overall heat transfer conductance UA can also be expressed as [35]:

$$\frac{1}{UA} = \left(\frac{1}{h_o A_o} + \frac{1}{h_i A_i} + R_{o,\text{ finned tube}} \right) \tag{6}$$

The first term on the right hand side of Eq. (6) describes the external convective heat resistance due to evaporation on the external surface of the tube, the second term is the internal convective heat resistance due to single-phase flow inside the tube, and the third term is the conductive heat resistance of the tube wall. To evaluate the internal convective resistance, h_i, needs to be
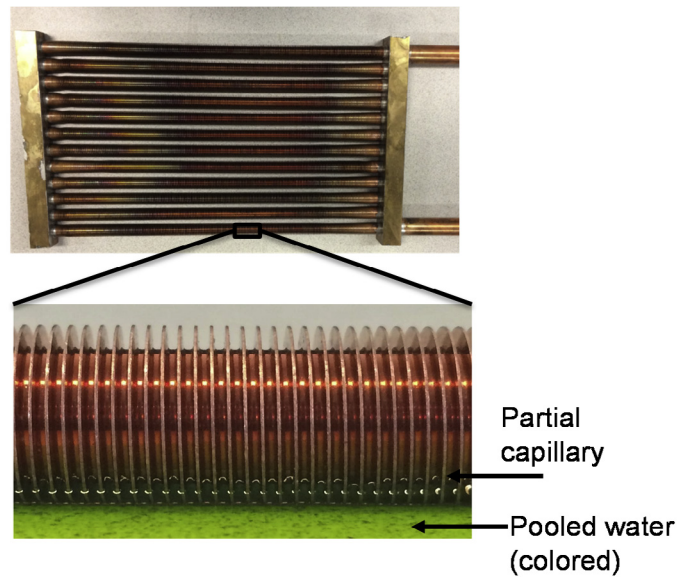
calculated. The flow of chilled water inside the tube is characterized by the Reynolds number, Re_i:

$$Re_i = \frac{\rho V D_{i,\text{tube}}}{\mu} \tag{7}$$

where, V is the chilled water velocity. For Reynolds numbers higher than 2300 ($2300 < Re_i < 5 \times 10^6$) Gnielinski correlation [35] can be used to calculate the Nusselt number:
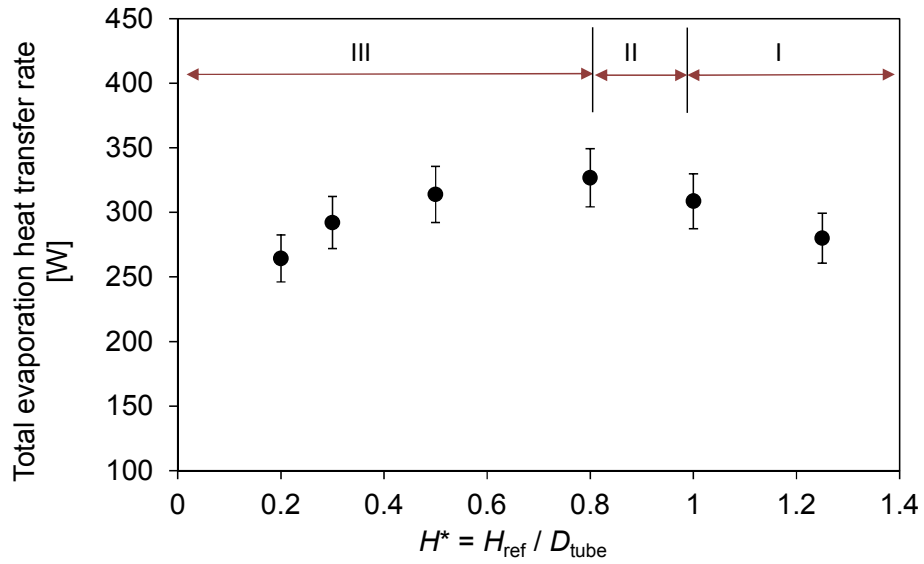
(a)

(b)

Fig. 5. (a) Total evaporation heat transfer rate, $\dot{Q}_{evap}$, versus the dimensionless height of the refrigerant, H*, and (b) custom-built low pressure evaporator showing partial capillary action.

$$Nu_i = \frac{\left(\frac{f}{2}\right)(Re_i - 1000)Pr_i}{1 + 12.7\left(\frac{f}{2}\right)^{0.5}\left(Pr_i^{2/3} - 1\right)} \qquad (8)$$

with

$$f = 0.078 Re_i^{-\frac{1}{4}} \qquad (9)$$

Finally, the internal heat transfer coefficient, h_i, is calculated as follows:

$$h_i = \frac{Nu_i \, k_{water}}{D_{i,tube}} \qquad (10)$$

Then the conductive heat resistance of the tube wall due to the fin resistance is calculated as explained in Appendix A and Eq. (6) is rewritten in order to obtain the external heat transfer coefficient (h_o) of the finned tubes:

$$h_o = \frac{1}{\left(\frac{1}{UA} - \frac{1}{h_i A_i} + R_{o, \text{ finned tube}}\right) A_o} \qquad (11)$$

However, the resistance of the finned tube $R_{o,\text{finned tube}}$ depends on the external heat transfer coefficient. Therefore, an iterative

(a)

(b)

Fig. 6. (a) Total evaporation heat transfer rate and (b) the overall heat transfer coefficient.

process is implemented to calculate h_o.

The coefficient of performance (COP) and specific cooling power (SCP) of the system are calculated to evaluate the performance of the chiller. The total evaporative cooling energy during adsorption and the total heat transfer to the adsorber beds during desorption are:

$$Q_e[J] = \int_{\text{adsorption}} \dot{m}_{in} c_p (T_{in} - T_{out}) dt \qquad (12)$$

$$Q_{\text{total heating}}[J] = \int_{\text{desorption}} \dot{m}_{hf} c_{p, hf} \left(T_{hf, \, in} - T_{hf, \, out}\right) dt \qquad (13)$$

where $\dot{m}_{hf}$ is the mass flow rate of heating fluid to adsorber beds, and $T_{hf, \, inlet}$ and $T_{hf, \, outlet}$ are the heating fluid inlet and outlet temperatures, respectively. The COP and SCP are:

$$COP = \frac{Q_e}{Q_{\text{total heating}}} \qquad (14)$$

$$SCP \, [W/kg] = \frac{Q_e}{m_{\text{adsorbent}} \tau_{\text{cycle}}} \qquad (15)$$

where $m_{\text{adsorbent}}$ is the mass of dry adsorbent inside the adsorber beds and τ_{cycle} is the cycle time (sum of adsorption and desorption times) given in Table 3.

4. Uncertainty analysis

The systematic uncertainty [36] in calculation of the overall heat transfer coefficient, U, was 1.1% and the random uncertainty in the measurement of U over time was 11%. Thus, the maximum uncertainty in the calculation of U was 12%. The detailed calculation of the total uncertainties for U is shown in Appendix B. The maximum uncertainties in the calculations of COP and SCP were 13% and 6.7%, respectively (see Appendix B).

5. Results and discussion

The operating pressure and temperature of the evaporator for a constant chilled water inlet temperature of 15 °C and a cycle time of 20 min are shown in Fig. 4. It can be seen in Fig. 4a that the dynamic behavior of the adsorption chiller is reproducible during two continuous cycles. At the beginning of the test ($t = 0$ s), all of the thermocouples have the same reading. Upon opening the control valve, the evaporation temperature is reduced to a value controlled by the suction pressure of the adsorber bed. Due to evaporation, heat is transferred from the chilled water to the liquid water refrigerant, and the chilled water temperature at the outlet of the evaporator is reduced, as shown in Fig. 4. $\dot{Q}_{evap}$ and U are calculated from the quasi-steady state section of the data as demarcated in grey in Fig. 4. In this region, U is evaluated using Eq. (3), even though the adsorption rate is lower in this region. It should be noted that log mean temperature difference (LMTD) formula was developed for steady state flow regimes. We also calculated the U for the first part of the adsorption and noticed that the difference in the U value compared to that of quasi-steady part was between 8% and 10%.

Fig. 5a shows the effect of liquid refrigerant height on $\dot{Q}_{evap}$ at a chilled water inlet temperature of 15 °C and a mass flow rate of 2.5 kg/min. $\dot{Q}_{evap}$ can be divided into three regions. In region I (H* > 1), tubes were fully submerged and the hydrostatic pressure affects the pool boiling in the following manner: i) the pressure
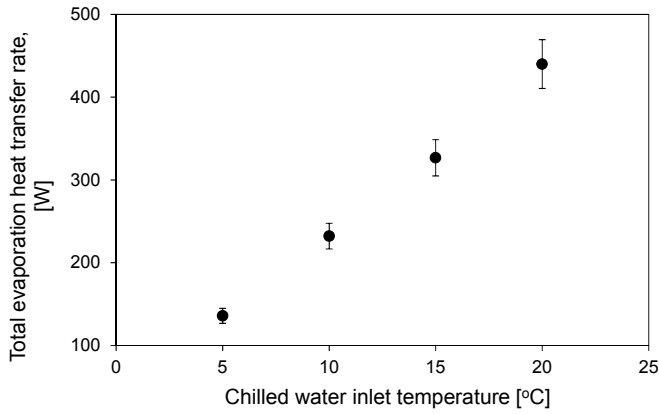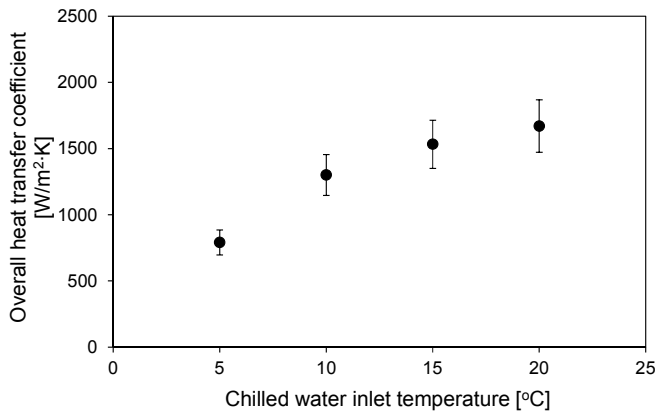
Table 4
Comparison of the evaporator tests.

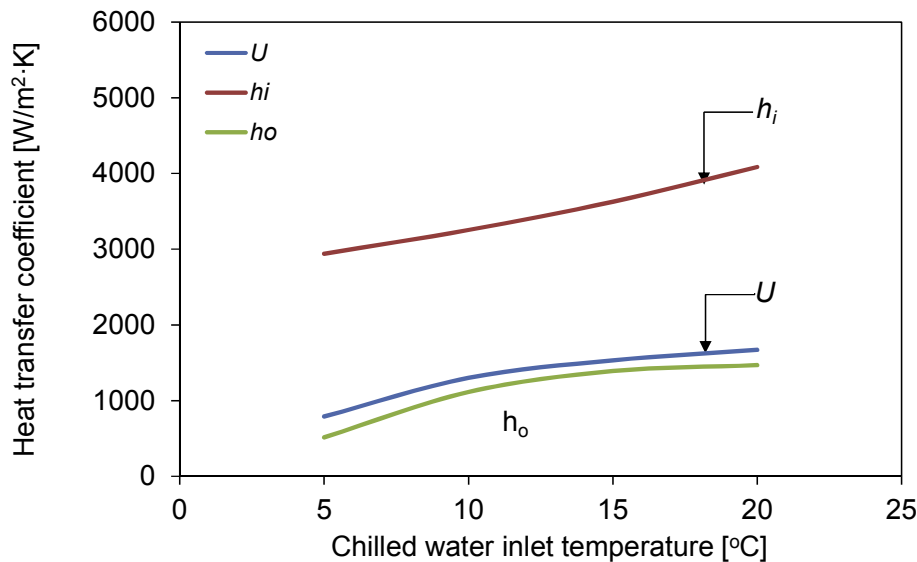| Chilled water inlet temperature (°C)	Evaporator tested using vacuum pump		Evaporator tested using adsorption chiller	
	Cooling capacity (W)	Overall heat transfer coefficient (W/m²·K)	Cooling capacity (W)	Overall heat transfer coefficient (W/m²·K)
10	243.1	1377.2	232.0	1300.1
15	346.3	1611.3	326.6	1532.4
20	461.2	1752.4	440.5	1670.5

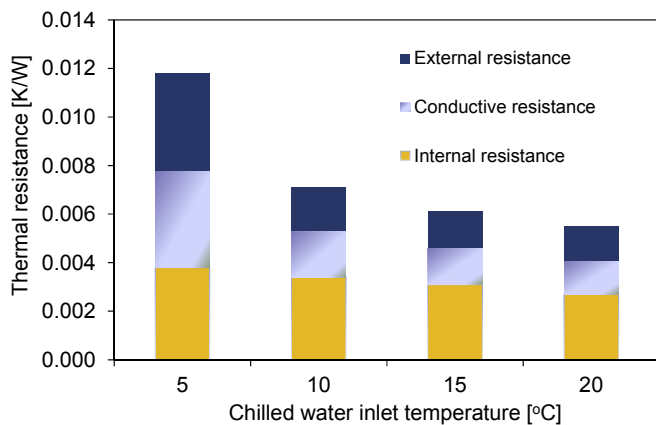**Fig. 7.** Heat transfer coefficients and the chilled water temperature at 2.5 kg/min.

Fig. 8. Comparison of thermal resistances in the evaporator for a chilled water mass flow rate of 2.5 kg/min.

gradient between the liquid water-vapor interface and the bottom of the evaporator increases causing the saturation temperature of water at the bottom of the evaporator to increase; ii) the temperature difference between the chilled water circulated inside the tubes and the refrigerant decreases, and thus, $\dot{Q}_{evap}$ reduces. In region II ($0.8 < H^* < 1$), the capillary action partly covers the outside surface of the tubes. Therefore, the optimum height for the liquid refrigerant filling is around $H^* = 0.8$. A maximum $\dot{Q}_{evap}$ of 326.6 W was achieved at $H^* = 0.8$. In region III ($H^* < 0.8$), the capillary force fails to overcome the gravity force and cover the entire surface of the tubes. Due to loss of heat transfer surface area, $\dot{Q}_{evap}$ in region III decreases.

The performance of the flooded evaporator was also tested for the optimum liquid refrigerant level at the chilled water inlet temperatures of 5, 10, 15, and 20 °C. The total heat transfer rates are compared in Fig. 6a. As the chilled water temperature increases from 5 °C to 20 °C, $\dot{Q}_{evap}$ increases from 135 W to 440 W. The wall superheat ΔT is a function of chilled water temperature (T_{inlet}). Increasing T_{inlet} enables a higher ΔT and thus a higher evaporation rate. The overall heat transfer coefficient, U, is plotted for different chilled water temperatures, T_{inlet}, in Fig. 6b. It can be seen that by increasing T_{inlet} from 5 °C to 20 °C, U increases from 790 to 1670 W/m²K. When T_{inlet} increases, it increases Re and decreases Pr due to decrease in the viscosity of water. This cumulative effect increases the Nu number. Therefore, the internal convection coefficient inside the tube increases. Increasing T_{inlet} results in a higher evaporation temperature and a lower viscosity of the liquid film around the tube. Therefore, the external convection coefficient around the tube increases as well. Thus, higher T_{inlet} enhances both internal and external convection coefficients, and as a result, the overall heat transfer coefficient.

Fig. 6 is the evaluation of the evaporator performance in a system coupled to the adsorber beds. We also tested this evaporator separately and independent of the adsorber beds. The evaporator when was tested using a vacuum pump instead of the adsorption chiller gave a similar performance (see Table 4). The test procedure was similar to procedure used by Thimmaiah et al. [24] and Lanzerath et al. [23]. The setup consisted of a TCS and a variable speed pump to provide a constant temperature chilled water to the evaporator at different mass flow rates. A control valve was used to regulate the pressure inside the evaporator. A vacuum pump and cold trap were used to mimic an adsorber bed. The comparison of the cooling powers and overall heat transfer coefficients achieved by using the evaporator installed in the adsorption chiller and that
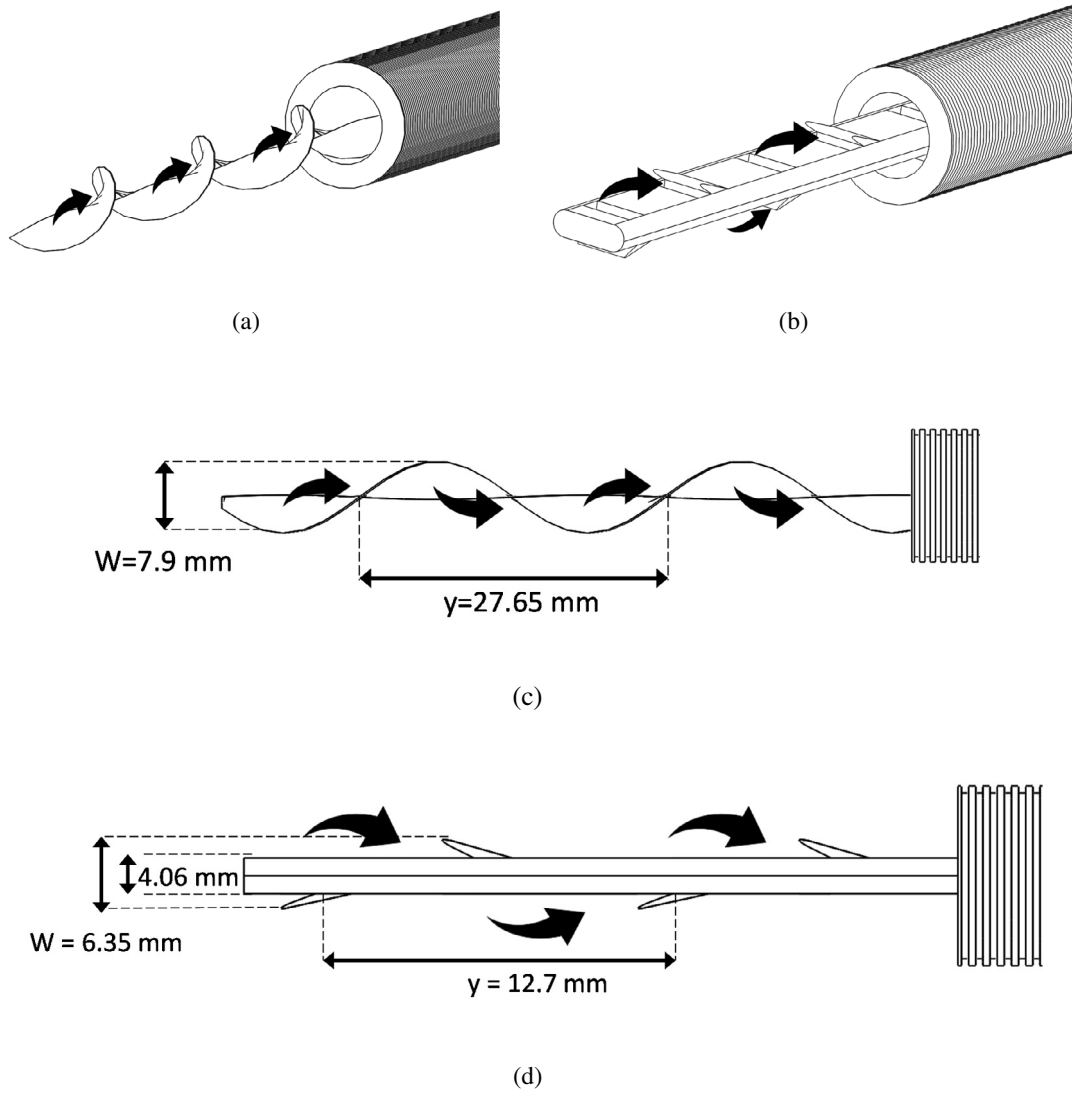
(a)   (b)

(c)

(d)

Fig. 9. Schematic of turbulent flow generators: (a) twisted tape and (b) Z-type. Geometrical details of (c) twisted tape and (d) Z-type turbulent flow generators.

(a)   (b)
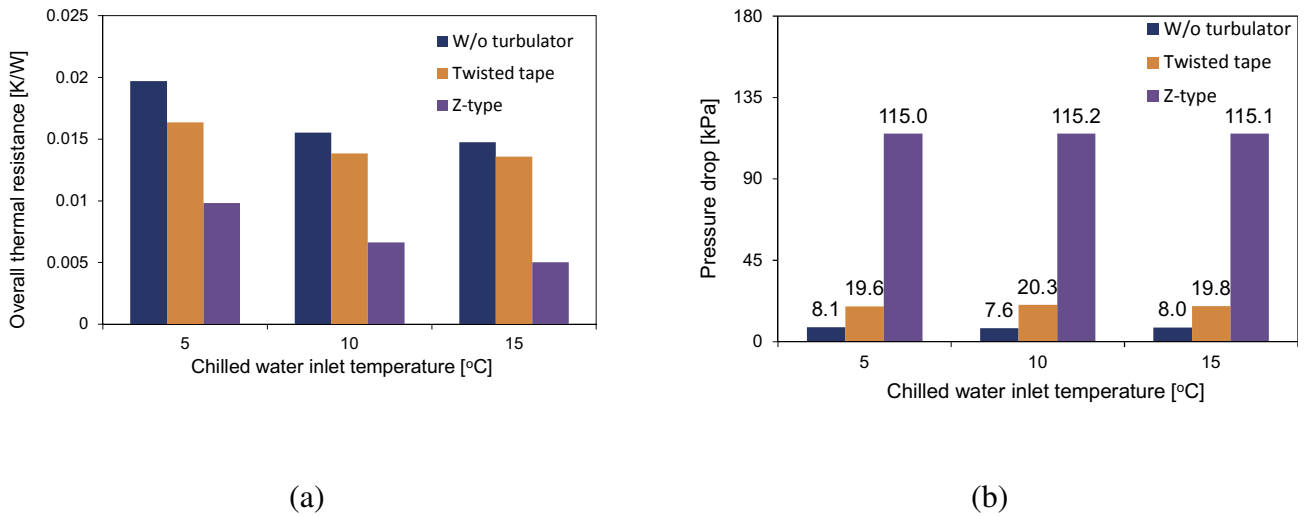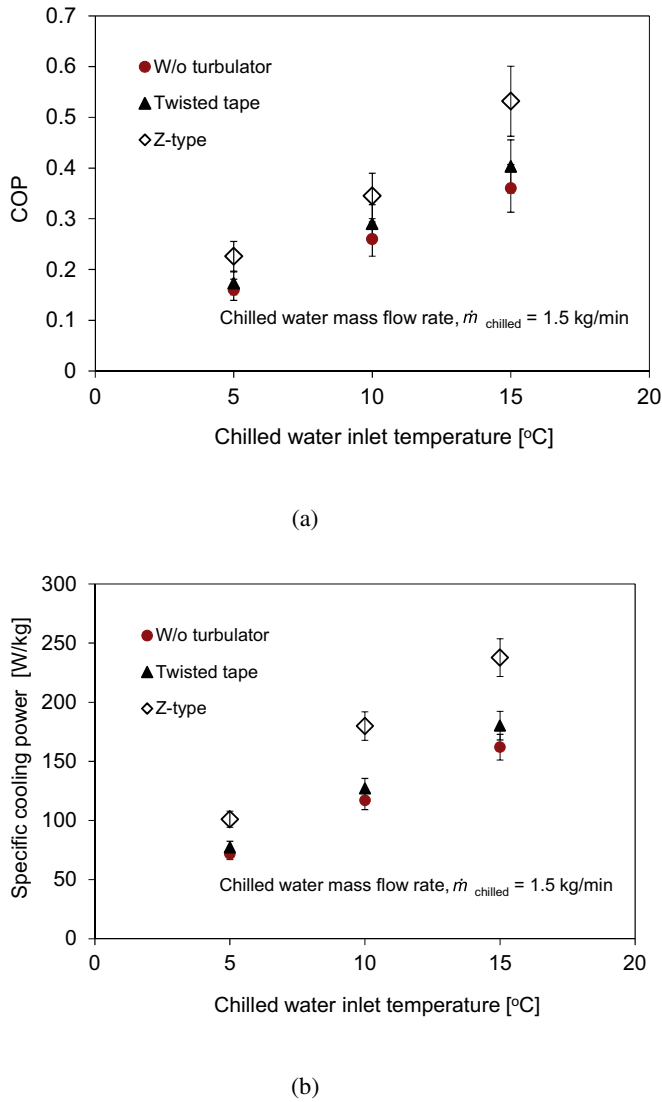
Fig. 10. Comparison between tubes without turbulators, and with twisted tape and Z-type turbulators for the chilled water mass flow rate of 1.5 kg/min: (a) overall thermal resistance and (b) pressure drop.

(a)

(b)

Fig. 11. Comparison of (a) COP and (b) SCP of adsorption chiller at the chilled water mass flow rate of 1.5 kg/min for the evaporator with and without turbulators.

tested independently shows less than a 6% difference under chilled water inlet temperatures of 10–20 °C.

In Fig. 7, the evaluated values for h_o, h_i, and U are plotted versus chilled water temperature for a chilled water mass flow rate of 2.5 kg/min. The convective heat transfer coefficients in the evaporator tubes are $h_i = 3627$ W/m^{2}K and $h_o = 1390$ W/m^{2}K at 15 °C. The internal convective coefficient (h_i) is 2.6 times higher than h_o. h_i is high due to the small ID of the tube, while the pool boiling results in a low h_o. The thermal resistances of the evaporator for a chilled water mass flow rate of 2.5 kg/min are shown in Fig. 8. As the chilled water inlet temperature varies from 5 to 20 °C, the internal

thermal resistance ($1/h_iA_i$) varies from 32% to 50% of the overall thermal resistance ($1/UA$), the conductive resistances ($R_{o, \text{finned tube}}$) is about 28%, and the external convective resistance ($1/h_oA_o$) decreases from 34% to 23%. The conductive resistances of enhanced tubes depend upon the overall fin efficiency ($\eta_{o, \text{fin}}$) and h_o. In Eq. (6), h_o appears in both external convective heat resistance and conductive heat transfer resistance due to the fins. Therefore, increasing h_o of the enhanced tubes can be favorable to reduce the overall resistance of the evaporator.

The internal thermal resistance dominates the $1/UA$ for chilled water temperatures from 10 to 20 °C, mainly due to the small internal heat transfer surface area of the tubes. For the chilled water temperature of 5 °C, $1/h_oA_o$ has the greatest influence on $1/UA$ due to the low saturation pressure of water at 5 °C.

To reduce the overall thermal resistance for any chilled water temperature, the internal resistance of the evaporator should be reduced. This can be achieved by incorporating turbulators, enhancing the internal heat transfer surface area, A_i, or increasing the mass flow rate. Increasing A_i for 7.9 mm ID tubes is not practical and increasing the mass flow rate results in a higher pressure drop and higher pumping power. Also, increasing the mass flow rate results in a lower temperature difference between the inlet and outlet of the evaporator. Therefore, to improve the thermal performance of the evaporator, two types of turbulent flow generators (twisted-tape [37] and Z-type) were tested.

Twisted tape turbulent flow generators were chosen based on the work of Piriyarungrod [37]. The incorporation of turbulent flow generators disrupts the flow and thermal boundary layer of the thermal fluid and produces vortices. A schematic of a twisted tape turbulent flow generators is shown in Fig. 9a with geometric details shown in Fig. 9c. The Z-type turbulent flow generator and its detailed geometry, designed with the help of Voss Manufacturing Inc. [38], are shown in Fig. 9b and d. Z-type turbulent flow generators further enhance the chaotic flow, particularly at low Re numbers. However, introducing inserts significantly increased the pressure drop in the evaporator tubes to the extent that the pump could no longer maintain the flow rate of 2.5 kg/min. Therefore, the following experiments were conducted at a mass flow rate of 1.5 kg/min.

A comparison of the thermal resistances and pressure drops of evaporators using twisted tape and Z-type turbulent flow generators are shown in Fig. 10. Twisted tape provides a 12% reduction in the overall thermal resistance and results in a 2.5 times higher pressure drop than that of tubes with no turbulators. Z-type inserts caused a 58% reduction in the overall thermal resistance while they resulted in a 14.5 times higher pressure drop. This significant pressure drop and more pump power must be considered in the overall design of an adsorption chiller.

The effect of the turbulent flow generators on the COP and SCP of the adsorption chiller are shown in Fig. 11. The tubes with twisted tape inserts provided, on average, a 10.5% improvement on the COP and a 9% improvement on the SCP of the chiller versus that with the tubes without turbulators. The tubes with Z-type turbulators provided, on average, a 41% improvement on the COP and a 47%

Table 5
Comparison between the cases with turbulators and without turbulators.

Case #	Turbulator type	Mass flow rate (kg/min)	Volumetric flow (m^3/s) V	Pressure drop (kPa) ΔP	Power consumption (W) P = ΔP*V	Increase in power consumption (%)	SCP (W/kg)	Increase in SCP (%)
1	–	1.5	2.33E-05	8	0.19	–	161.9	–
2	–	2.5	5.80E-05	7.9	0.46	142	233.7	44.3
3	twisted-tape	1.5	2.33E-05	19.8	0.46	142	180.2	11.3
4	Z-type	1.5	2.33E-05	115	2.68	1310	237.7	46.8
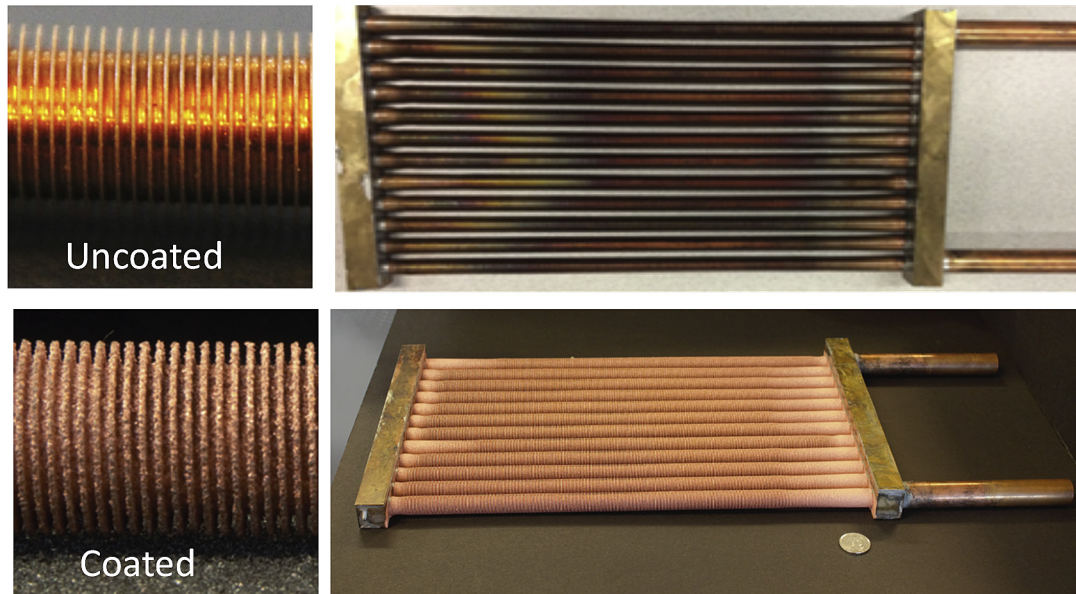
Fig. 12. Photographs of uncoated (UE) and coated evaporators (CE).
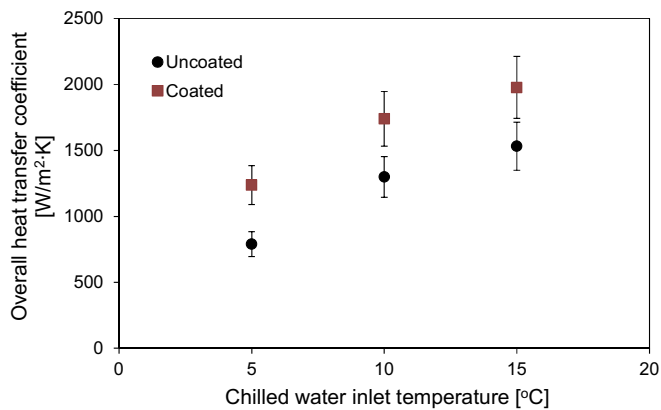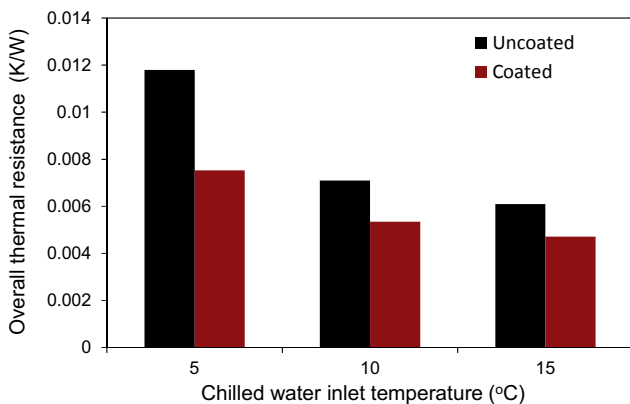
improvement on the SCP. However, Z-type turbulent flow generators resulted in an average pressure drop of 115 kPa (14.5 times higher than tubes with no turbulator). Higher pressure drop increases the adsorption chillers overall energy consumption (see Table 5).

Since the external thermal resistance shown in Fig. 8 corresponds to up to 34% of the overall thermal resistance, and a higher h_o reduces the fin thermal resistance, R_{fin}, the utilization of porous copper coating on the external fins needs to be exploited to further increase the COP and SCP of the adsorption chillers. It was shown theoretically and experimentally that the application of a porous coating to the finned surface has a positive effect on the heat transfer coefficient [23,39]. The photos of the coated evaporator (CE) and uncoated evaporator (UE) are shown in Fig. 12.

The performance of the porous copper CE was tested at the liquid refrigerant level (H* = 0.5) and a mass flow rate of 2.5 kg/min at the chilled water inlet temperatures of 5, 10, and 15 °C. The overall heat transfer coefficients of UE and CE are compared in Fig. 13a. It can be seen that by increasing T_{inlet} from 5 °C to 15 °C, U of the CE increases from 1237 to 1978 W/m^{2}K. In addition, U of the CE is 40% higher than the U of the UE. A comparison of the thermal resistances of UE and CE is shown in Fig. 13b. CE caused, on average, a 92% drop in overall thermal resistances over the UE. Schnabel et al. [40], achieved a 2.5-times higher total heat transfer with galvanic coating of plain tubes compared to uncoated tubes and according to their study, internal heat transfer limited the overall U. The thermal coated evaporator examined at chilled water mass flow rate of 16 kg/min in the work of Lanzerath et al. [23] enhanced the overall U by 50% compared to the uncoated finned tubes. By contrast, at low chilled water mass flow rate of 2.5 kg/min, the CE examined in this work enhanced the overall U by 30%.

The effect of the CE on the COP and SCP of the adsorption chiller are shown in Fig. 14. CE provided, on average, a 20% improvement on the COP and a 47.6% improvement on the SCP of the chiller versus UE. While, the pressure drop of the system remained unchanged similar to UE.
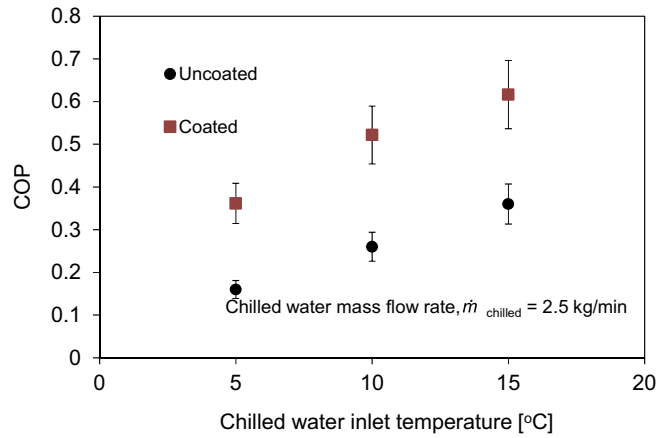

(a)

(b)

Fig. 13. Comparison of (a) overall heat transfer coefficient and (b) overall thermal resistance at the chilled water mass flow rate of 2.5 kg/min.

6. Conclusion

An LP flooded evaporator was built with 12 passes of horizontal

(a)
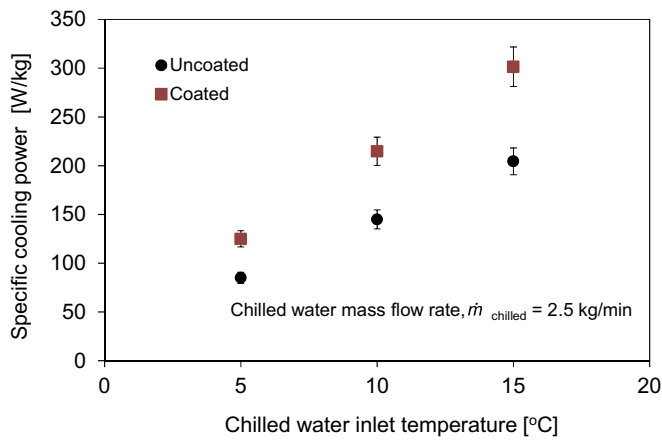
(b)

Fig. 14. Comparison of (a) COP and (b) SCP of adsorption chiller at the chilled water mass flow rate of 2.5 kg/min.

tubes immersed in a pool of water. Reducing the height of liquid refrigerant below the optimum height (0.8 times of the tube diameter) had a negative effect on the cooling power of the flooded evaporator. The main bottleneck to the thermal performance of the flooded evaporator was the internal heat transfer. Therefore, two different turbulent flow generators (twisted tape and Z-type) were inserted into the evaporator tubes. The insert turbulators resulted in a significant improvement in both specific cooling power (SCP) and coefficient of performance (COP) of the adsorption chiller. However, they created a large pressure drop for the chilled water side. The main findings of this study were summarized as follows:

- The optimum height for the liquid filling was H^* of 0.8 which provided the highest cooling power of 326.6 W.
- The overall heat transfer coefficient, U, of the evaporator at optimum liquid level was 1500 W/m²K.
- The internal thermal resistance contributed to up to 50% of the overall resistance.
- The conductive and external convective resistances, on average, contributed to 32% and 25% of the overall thermal resistance, respectively.

- Twisted tape turbulent flow generator provided an average of 12% reduction in the overall thermal resistance and a 20 kPa increase in the pressure drop.
- Z-type turbulent flow generator provided an average of 58% reduction in the overall thermal resistance of the evaporator and a 115 kPa increase in pressure drop.
- Twisted tape provided an average of 10.5% and 9% improvement on the COP and SCP, and Z-type provided an average of 41% and 47% improvement on the COP and SCP of the adsorption chiller, respectively.
- Porous copper coatings were employed on the outside surface of the evaporator tubes to improve the flooded evaporator performance.
- The overall heat transfer of the coated evaporator was increased by 1.4 times compared to that of the uncoated evaporator.
- The coated evaporator improved the average SCP of the adsorption chiller by 47.6%.

Acknowledgment

Appendix A

The tubes of interest in this study have circumferential, rectangular cross-section fins. The efficiency of a fin located on the surface of the tube with circumferential, rectangular cross-section fins can be calculated by Ref. [35]

$$\eta_f = C \left(\frac{K_1(mr_1)I_1(mr_{2c}) - I_1(mr_1)K_1(mr_{2c})}{I_0(mr_1)K_1(mr_{2c}) + K_0(mr_1)I_1(mr_{2c})} \right) \tag{A1}$$

where

$$C = \frac{(2r_1/m)}{(r_{2c}^2 - r_1^2)} \tag{A2}$$

$$m = \sqrt{\left(\frac{2h_o}{k_{copper}t_f} \right)} \tag{A3}$$

$$r_{2c} = r_2 + \left(t_f / 2 \right) \tag{A4}$$

$$A_f = 2\pi \left(r_{2c}^2 - r_1^2 \right) \tag{A5}$$

and r_1 and r_2 are the distances from the center of the tube to the fin base and fin tip, respectively, I_0, and K_0 are the modified, zero-order Bessel functions of the first and second kinds, respectively, I_1, and K_1 are the modified, first-order Bessel functions of the first and second kinds, respectively, t_f is the fin thickness and A_f is the fin heat transfer surface area.

The total external heat transfer surface area of the finned tube is

$$A_t = N\left(A_f + A_b\right) \tag{A6}$$

where N is the total number of fins, A_b is the prime (plain exposed portion of the base) heat transfer surface area of the finned tube, t_b is the space between two fins and

$$A_b = 2\pi r_1 t_b \tag{A7}$$

Using Eqs. (A1), (A5), and (A6), the overall efficiency of the finned tube can be calculated [35]:

$$\eta_{o,\,fin} = 1 - \frac{A_f}{A_f + A_b}\left(1 - \eta_f\right) \tag{A8}$$

Consequently, the conductive heat transfer resistance due to the fins of the finned tube is

$$R_{fin} = \frac{1}{\eta_{o,\,fin} h_o A_t} \tag{A9}$$

In addition, the conductive resistance of wall located under the fins is

$$R_{wall} = \frac{\ln(r_1/r_0)}{2\pi k_{copper} L} \tag{A10}$$

where r_0 and L are the internal radius and length of the finned tube, respectively. R_{fin} and R_{wall} are thermal resistances in series. Therefore, the overall conductive resistance of the finned tube is

$$R_{o,\,finned\ tube} = R_{fin} + R_{wall} \tag{A11}$$

Information required in calculating the overall resistance of the evaporator is listed in Table A1.

Table A1
Detailed geometry of the evaporator tube.

Parameter	GEWA®-K-2615
L	3.6 m
r_0	3.95×10^{-3} m
r_1	4.75×10^{-3} m
r_2	6.25×10^{-3} m
t_f	3.00×10^{-4} m
t_b	7.00×10^{-4} m
k_{copper}	340 W/m·K
A_t	0.491 m^2
A_i	0.089 m^2

Appendix B

The systematic uncertainty [36] in the evaporator heat transfer rate calculation is:

$$\left(\frac{\delta \dot{q}_e}{\dot{q}_e}\right)_{systematic} = \sqrt{\left(\frac{\delta \dot{m}_{in}}{\dot{m}_{in}}\right)^2 + \left(\frac{\delta(T_{in} - T_{out})}{T_{in} - T_{out}}\right)^2} \tag{B1}$$

where,

$$\frac{\delta(T_{in} - T_{out})}{T_{in} - T_{out}} = \sqrt{\left(\frac{\delta T_{in}}{T_{in}}\right)^2 + \left(\frac{\delta T_{out}}{T_{out}}\right)^2} = \sqrt{0.0075^2 + 0.0075^2}$$
$$= 0.01 \tag{B2}$$

Thus, the maximum systematic uncertainty in the calculation of evaporator heat transfer rate is:

$$\left(\frac{\delta \dot{q}_e}{\dot{q}_e}\right)_{systematic} \times 100 = \sqrt{0.005^2 + 0.01^2} = 1.1\% \tag{B3}$$

Also, the standard deviation for $\dot{q}_e$ due to the random uncertainty is 5.6%. Thus the maximum uncertainty of $\dot{q}_e$ during the experiments is 6.7% ($= 1.1\% + 5.6\%$). Eq. (B4) gives the systematic uncertainty of the overall heat transfer coefficient:

$$\left(\frac{\delta U}{U}\right)_{systematic} = \sqrt{\left(\frac{\delta \dot{Q}_e}{\dot{Q}_e}\right)_{systematic}^2 + \left(\frac{\delta\,\Delta T_{LMTD}}{\Delta T_{LMTD}}\right)^2} \tag{B4}$$

where $\left(\frac{\delta \dot{Q}_e}{\dot{Q}_e}\right)_{systematic}$ and $\frac{\delta\,\Delta T_{LMTD}}{\Delta T_{LMTD}}$ are equal to 1.1% and 0.04%, respectively. Therefore, $\left(\frac{\delta U}{U}\right)_{systematic}$ is equal to 1.1% ($\approx (1.1\% + 0.04\%)$. The random uncertainty in the measurement of U over time is 10.8%. Thus, the maximum uncertainty in the calculation of overall heat transfer coefficient is 11.9% ($= 1.1\% + 10.8\%$). Similarly, the maximum uncertainty in the calculation of $Q_{total\ heating}$ was 11.1% ($= 1.1\% + 10\%$). Therefore, the maximum uncertainties in the calculations of COP and SCP were as follows:

$$\frac{\delta COP}{COP} \times 100 = \sqrt{\left(\frac{\delta Q_e}{Q_e}\right)^2 + \left(\frac{\delta Q_{total\ heating}}{Q_{total\ heating}}\right)^2} \times 100$$
$$= \sqrt{0.067^2 + 0.111^2} \times 100 = 12.9\% \tag{B5}$$

$$\frac{\delta SCP}{SCP} \times 100 = \sqrt{\left(\frac{\delta Q_e}{Q_e}\right)^2 + \left(\frac{\delta m_{adsorbent}}{m_{adsorbent}}\right)^2 + \left(\frac{\delta \tau_{cycle}}{\tau_{cycle}}\right)^2} \times 100$$
$$= \sqrt{0.067^2 + \left(\frac{1}{700}\right)^2 + \left(\frac{1}{1200}\right)^2} \times 100 = 6.7\% \tag{B6}$$

Nomenclature

A	heat transfer surface area (m^2)
A/C	air conditioning
β	coefficient of cubic expansion (K^{-1})
c_p	heat capacity at constant pressure (J/kg K)
COP	coefficient of performance
ΔT	wall superheat (K)
ΔT_{LM}	log mean temperature difference (K)
D	diameter (m)
f	friction factor
γ	gamma angle (rad)
g	standard gravity (m/s^2)
Gr	Grashof number
H	height (m)
h	heat transfer coefficient (W/m^2 K)
HFC	hydrofluorocarbon refrigerants
HVAC	heating, ventilation and air-conditioning
ICE	internal combustion engine
ID	internal diameter (m)
k	thermal conductivity (W/m K)
L	length of the tube (m)
LP	low pressure
m	mass (kg)

$\dot{m}$	mass flow rate (kg/s)
NTU	number of transfer units
Nu	Nusselt number
OD	outer diameter (m)
P	pressure (Pa)
Pr	Prandlt number
$\dot{Q}$	total heat transfer rate (W)
$\dot{q}$	heat transfer rate (W)
R	Resistance (K/W)
r	radius (m)
Re	Reynolds number
ρ	density (kg/m^3)
T	temperature (°C)
TCS	temperature control system
τ t	cycle time (s) time (s)
ν	kinematic viscosity (m^2/s)
U	overall heat transfer coefficient (W/m^2 K)
V	velocity (m/s)
VCR	vapor compression refrigeration cycle

Subscripts

ads	adsorbent
chilled	chilled water
copper	copper tube
e	Evaporator
finned	finned tube
i	in
in	inlet chilled water
o	out
out	outlet chilled water
pitch	pitch of the finned tube
ref	refrigerant
sat	saturation
tube	evaporator tube
vap	vapor
wall	tube wall
water	evaporating water

Superscript

*	Dimensionless

References

[1] Goetzler BYW, Ashrae M, Zogg R, Ashrae M, Young JIM, Ashrae AM, et al. Alternatives to HVAC technology. ASHRAE J 2014:12–23.

[2] Goetzler William, Zogg Robert, Jim Young CJ. Energy savings potential and RD & D opportunities for non- vapor-compression HVAC. Energy Effic Renew Energy 2014:3673.

[3] Government of Canada. Learn the facts Air conditioning and its effect on fuel consumption. Nat Resour Can 2016. http://www.nrcan.gc.ca/energy/efficiency/transportation/cars-light-trucks/buying/16740 [Accessed 01 January 2017].

[4] Suzuki M. Application of adsorption cooling systems to automobiles. Heat Recover Syst CHP 1993;13:335–40.

[5] Farrington R, Rugh J. Impact of vehicle air-conditioning on fuel economy, tailpipe emissions, and electric vehicle range. Fuel 2000. doi:NREL/CP-540-28960, http://www.nrel.gov/docs/fy00osti/28960.pdf.

[6] Sumathy K, Yeung KH, Yong L. Technology development in the solar adsorption refrigeration systems. Prog Energy Combust Sci 2003;29:301–27. http://dx.doi.org/10.1016/S0360-1285(03)00028-5.

[7] Jiangzhou S, Wang RZ, Lu YZ, Xu YX, Wu JY, Li ZH. Locomotive driver cabin adsorption air-conditioner. Renew Energy 2003;28:1659–70. http://dx.doi.org/10.1016/S0960-1481(03)00007-7.

[8] Wang RZ, Oliveira RG. Adsorption refrigeration-An efficient way to make good use of waste heat and solar energy. Prog Energy Combust Sci 2006;32:424–58. http://dx.doi.org/10.1016/j.pecs.2006.01.002.

[9] Goyal P, Baredar P, Mittal A, Siddiqui AR. Adsorption refrigeration technology - an overview of theory and its solar energy applications. Renew Sustain Energy Rev 2016;53:1389–410. http://dx.doi.org/10.1016/j.rser.2015.09.027.

[10] Wang LW, Wang RZ, Oliveira RG. A review on adsorption working pairs for refrigeration. Renew Sustain Energy Rev 2009;13:518–34. http://dx.doi.org/10.1016/j.rser.2007.12.002.

[11] Sharafian A, Nemati Mehr SM, Huttema W, Bahrami M. Effects of different adsorber bed designs on in-situ water uptake rate measurements of AQSOA FAM-Z02 for vehicle air conditioning applications. Appl Therm Eng 5 April 2016;98:568–74. http://dx.doi.org/10.1016/j.applthermaleng.2015.12.060.

[12] Sharafian A, Dan PC, Huttema W, Bahrami M. Performance analysis of a novel expansion valve and control valves designed for a waste heat-driven two-adsorber bed adsorption cooling system. Appl Therm Eng 5 May 2016;100:1119–29. http://dx.doi.org/10.1016/j.applthermaleng.2016.02.118.

[13] Demir H, Mobedi M, Ülkü S. A review on adsorption heat pump: problems and solutions. Renew Sustain Energy Rev 2008;12:2381–403. http://dx.doi.org/10.1016/j.rser.2007.06.005.

[14] Schnabel L, Witte K, Kowol J, Schossig P. Evaluation of different evaporator concepts for thermally driven sorption heat pumps and chiller. In: Int. sorption heat pump conf., Padua, Italy; 2011. p. 525–43.

[15] Giraud F, Rulliere R, Toublanc C, Clausse M, Bonjour J. Experimental evidence of a new regime for boiling of water at subatmospheric pressure. Exp Therm Fluid Sci 2014;60:45–53. http://dx.doi.org/10.1016/j.expthermflusci.2014.07.011.

[16] Castro J, Oliva A, Perez-Segarra CD, Oliet C. Modelling of the heat exchangers of a small capacity, hot water driven, air-cooled H2O-LiBr absorption cooling machine. Int J Refrig 2008;31:75–86. http://dx.doi.org/10.1016/j.ijrefrig.2007.05.019.

[17] Florides GA, Kalogirou SA, Tassou SA, Wrobel LC. Design and construction of a LiBr-water absorption machine. Energy Convers Manag 2003;44:2483–508. http://dx.doi.org/10.1016/S0196-8904(03)00006-2.

[18] Li W, Wu XY, Luo Z, Webb RL. Falling water film evaporation on newly-designed enhanced tube bundles. Int J Heat Mass Transf 2011;54:2990–7. http://dx.doi.org/10.1016/j.ijheatmasstransfer.2011.02.052.

[19] Sabir HM, Elhag YBM. Experimental study of capillary-assisted evaporators. Appl Energy 2008;40:399–407. http://dx.doi.org/10.1016/j.enbuild.2007.02.036.

[20] Sabir HM, Bwalya AC. Experimental study of capillary-assisted water evaporators for vapour-absorption systems. Appl Energy 2002;71:45–57. http://dx.doi.org/10.1016/S0306-2619(01)00042-3.

[21] Sabir HM, ElHag YBM. A study of capillary-assisted evaporators. Appl Therm Eng 2007;27:1555–64. http://dx.doi.org/10.1016/j.applthermaleng.2006.09.011.

[22] Xia ZZ, Yang GZ, Wang RZ. Experimental investigation of capillary-assisted evaporation on the outside surface of horizontal tubes. Int J Heat Mass Transf 2008;51:4047–54. http://dx.doi.org/10.1016/j.ijheatmasstransfer.2007.11.042.

[23] Lanzerath F, Seiler J, Erdogan M, Schreiber H, Steinhilber M, Bardow A. The impact of filling level resolved: capillary-assisted evaporation of water for adsorption heat pumps. Appl Therm Eng 2016;102:513–9. http://dx.doi.org/10.1016/j.applthermaleng.2016.03.052.

[24] Cheppudira Thimmaiah P, Sharafian A, Huttema W, Bahrami M. Effects of capillary-assisted tubes with different fin geometries on the performance of a low-operating pressure evaporator for adsorption cooling systems. Appl Energy 2015:171. http://dx.doi.org/10.1016/j.apenergy.2016.03.070.

[25] Castro J, Farns J, Oliva A, Garca-Rivera E. Flooded evaporators for LiBr-H2O absorption chillers: modelling and validation. In: Proc. 8th IIR Gustav Lorentzen Nat. Work. Fluids Conf; 2008. p. 217–23.

[26] Thome JR. Falling film evaporation: state-of-the-art review of recent work. J Enhanc Heat Transf 1999;6:263–77.

[27] Ribatski G, Jacobi AM. Falling-film evaporation on horizontal tubes - a critical review. Int J Refrig 2005;28:635–53. http://dx.doi.org/10.1016/j.ijrefrig.2004.12.002.

[28] Li W, Wu XY, Luo Z, Yao SC, Xu JL. Heat transfer characteristics of falling film evaporation on horizontal tube arrays. Int J Heat Mass Transf 2011;54:1986–93. http://dx.doi.org/10.1016/j.ijheatmasstransfer.2010.12.031.

[29] Wang RZ, Xia ZZ, Wang LW, Lu ZS, Li SL, Li TX, et al. Heat transfer design in adsorption refrigeration systems for efficient use of low-grade thermal energy. Energy 2011;36:5425–39. http://dx.doi.org/10.1016/j.energy.2011.07.008.

[30] Cheppudira Thimmaiah P, Sharafian A, Huttema W, Bahrami M. Effects of capillary-assisted tubes with different fin geometries on the performance of a low-operating pressure evaporator for adsorption cooling systems. Appl Energy 1 June 2016;171:256–65. http://dx.doi.org/10.1016/j.apenergy.2016.03.070.

[31] Thimmaiah PC, Sharafian A, Huttema W, Dhillon A, Bahrami M. Performance of finned tubes used in low-pressure capillary-assisted evaporator of adsorption cooling system. Appl Therm Eng 5 August 2016;106:371–80.

[32] Giraud F, Toublanc C, Rullière R, Bonjour J, Clausse M. Experimental study of water vaporization occurring inside a channel of a smooth plate-type heat exchanger at subatmospheric pressure. Appl Therm Eng 2016;106:180–91. http://dx.doi.org/10.1016/j.applthermaleng.2016.05.151.

[33] Sharafian A, Nemati Mehr S, Thimmaiah P, Huttema W, MB. Effects of adsorbent mass and number of adsorber beds on the performance of a waste-heat driven adsorption cooling system for vehicle air conditioning applications. Energy 1 October 2016;112:481–93.

[34] H JP. Heat transfer. tenth ed. McGraw-Hill Education; 2010.

[35] Bergman Theodore L, Lavine Adrienne S, Frank P, Incropera DPD. One-dimensional, steady-state conduction. vol. Fundamenta. John WIiley & Sons, Inc; 2014. http://dx.doi.org/10.1007/s13398-014-0173-7.2.

[36] Holman JP. Experimental methods for engineers. eighth ed. McGraw-Hill Series in Mechanical Engineering; 2012.

[37] Piriyarungrod N, Eiamsa-ard S, Thianpong C, Pimsarn M, Nanan K. Heat transfer enhancement by tapered twisted tape inserts. Chem Eng Process Process Intensif 2015;96:62–71. http://dx.doi.org/10.1016/j.cep.2015.08.002.

[38] Bob Carlo. Voss Mfg. Inc. Heat transfer tooling and equipment. 2016. www.vossmfg.com [Accessed 1 January 2016].

[39] Vasil'ev LL, Grakovich LP, Rabetskii MI, Tulin DV. Investigation of heat transfer by evaporation in capillary grooves with a porous coating. J Eng Phys Thermophys 2012;85:407–14. http://dx.doi.org/10.1007/s10891-012-0666-1.

[40] Schnabel L, Witte KT. Water as refrigerant - evaporator development for cooling applications. In: Heat powered cycles conf. proc; 2009.